Geophysical Research Letters

Supporting Information for

Basal crevasse formation on Byrd Glacier, East Antarctica as proxy for past subglacial flooding events

Sarah F. Child [1,2], Leigh A. Stearns [1,3], C. J. van der Veen [4], Pedro Elosegui [5,6]

1. Department of Geology, University of Kansas, Lawrence, KS 66045, USA

2. Cooperative Institute for Research in Environmental Sciences, University of Colorado, Boulder, CO580309, USA

3. Center for Remote Sensing of Ice Sheets, University of Kansas, Lawrence, KS 66045, USA

4. Department of Geography & Atmospheric Sciences, University of Kansas, Lawrence, KS 66045, USA

5. Massachusetts Institute of Technology, Haystack Observatory, Westford, MA, 01886 USA

6. Institute of Marine Sciences, ICM-CSIC, Barcelona, Spain, 08003

Contents of this file

Introduction

The following text is additional information about the models and data used in the main manuscript. We expand more on the GPS data, how the hydrostatic equilibrium boundary was determined, how ice thickness was estimated from surface elevation and bed topography data, the effect varying strain rates has on LEFM results, the route of subglacial water within the Byrd Glacier catchment, and tables of the data used in this research.

Text S1. GPS data

We collected geodetic-quality GPS data at a total of 26 locations on Byrd Glacier and three additional sites on surrounding bedrock (Figure S1) over three austral summer campaigns between November 2010 and January 2013. All the sites were equipped with Trimble (NetR9, 5700, or R7) receivers and Trimble Zephyr (55971.00 or 41249.00) antennae—brand and make

names are mentioned for identification purposes only. Most of the analysis presented here is based on dual-frequency carrier-beat phase observations collected at nine of the GPS sites straddling the glacier's grounding line over five days in December 2011, with a sampling rate of 30 s.

We used the GIPSY software package (Lichten and Boarder 1987) and high-precision kinematic data processing methods (e.g., Elosegui et al., (1996, 2006)) to estimate glacier GPS sites' time-varying positions once every 300 s. Precise satellite orbits from the International GNSS Service (IGS) were employed with no further orbit improvement. For each 300 s epoch, we estimated receiver clock errors, modeled as white noise stochastic process, as well as atmospheric zenith delays and the motion of the moving antenna, with the last two set of parameters modeled as random walk stochastic processes. Only observations above a minimum elevation angle of 7° were used.

The GPS analysis provides, among other parameters, stochastic-filter-smoothed time-dependent adjustments to the *a priori* values of the three-dimensional position parameters for each site. These adjustments (less a mean) are shown for nine of the GPS sites in Figure 1C for the vertical component of site position in a topocentric frame, e.g., a frame defined by the *a priori* position of the site in which the adjustments are expressed as relative position with cartesian components east, north, and vertical (positive up). The sites down-glacier from the grounding line exhibit dominant vertical position diurnal variations that can reach up to ~1 m peak-to-peak, indicative of tidal influences. The estimated formal uncertainties of vertical positions for the nine GPS sites range was 2—5 cm over the 3-month austral summer deployment of 2011/2012. The weighted root-mean-square (rms) scatter of vertical position estimates are derived from the weighted mean of the three rock sites over the entire deployment time (~2.25 years). Although the rock sites are obviously static, their GPS data were also processed using the same high-precision kinematic technique applied to the glacier sites hence providing an estimate of positioning precision for the latter.

Text S2. Hydrostatic Equilibrium

The hydrostatic equilibrium (H_e) was estimated using the buoyancy calculation,

$$H_e = h - \left(H * \left[\frac{\rho_w - \rho_i}{\rho_w}\right]\right) \quad (1)$$

where h is the present-day surface elevation, H is the ice thickness, and ρ_i, ρ_w are the ice and water density, respectively. The down-flow extent of the grounding zone is located where this value is approximately zero (when h is projected in orthometric heights) and ice begins to float. The data used for these parameters (h and H) are described below.

Text S3. Ice thickness data

Ice thickness was calculated by subtracting the picked CReSIS echogram bed topography from

the surface elevation data, described below. Both data sets were converted from their WGS84 ellipsoidal heights to orthometric ones using the EGM2008 model (Pavlis et al., 2012).

Bed elevation
The bed elevation is point data from the manually picked CReSIS echograms CReSIS, which is available from their L3 product of Byrd Glacier. The bed elevation is referenced vertically to the WGS84 ellipsoid and horizontally in WGS84 polar stereographic. Sources of error in the point data come from the geolocation of the airborne platform uncertainties, range measurement uncertainties, and bed interpretation error of echogram picking (Gogineni et al., 2014). Crossover analysis of overlapping flight paths resulted in a mean ice thickness error of ~30.64 m with a standard deviation of ~39.88 m (CReSIS, 2014, Gogineni et al., 2014).

Surface elevation
Our surface DEM is from 25 2 m resolution DEM strips generated from WorldView 1, 2, 3 imagery using the Surface Extraction with TIN-based Search-space Minimization (SETSM) algorithm by Noh and Howat (2015). For imagery collected at low degrees of off-nadir over regions with a high density of ground control, the accuracy of these products is assessed at ~1 m (Howat et al. 2019). Over Byrd Glacier, the off-nadir angle varied from 6º—29º and ground control is sparse, so the error is likely higher than the Howat et al. (2019) estimate and we assume a value of 5 m like that of Glennie (2018). We found in the 2 m DEMs that blunders existed from cloud cover, shadows, and the backside of terrain where image acquisition was impossible due to off-nadir (e.g. >20°) collection. These blunders were manually clipped from the DEMs and then each strip was coregistered to its closest neighbor upstream using the Nuth and Kääb (2011) method in McNabb (2019)'s python module PyBob. This method of co-registering was a means of maintaining a cohesive data registration before the strips were mosaicked to a grid of 5 m and referenced to the WGS84 ellipsoid.

Text S4. Velocity Data

Byrd Glacier Velocities
The velocity data for a non-flooding period were calculated from band 4 of Landsat 4 TM imagery collected in 1989 and 1990 (Stearns, 2007). The velocities from a flooding period are from Stearns et. al, (2008) and estimated from ASTER and ALOS AVNIR-2 data (collected from 2005-2007). Both sets were and processed in the Image Cross-Correlation (IMCORR) software which uses a feature tracking algorithm to determine the magnitude and direction of displacement (Scambos et. al., 1992) (see Figure S4).

Ross Ice Shelf Velocities
The feature tracking estimations were conducted using a mosaic of glacier surface velocities generated from Landsat 8 OLI imagery called the Landsat Ice Speed of Antarctica (LISA) (Scambos et al., 2019). Velocities were estimated using a feature tracking program called PyBob (Fahnestock et al., 2016). LISA mosaics have a spatial resolution of 750 m and the velocities used in the mosaic for this study were from imagery acquired over July 1, 2016 to April 30, 2017.

Text S5. The effect of increased strain rates on LEFM results

No radar data was collected during the flood period of 2005-2007, so we were unable to measure any newly formed basal crevasses during this time period. We instead used LEFM to model estimated basal crevasse heights based on surface velocities from a time of increased speeds and a time of normal ice flow. LEFM is an appropriate model to use in this circumstance because the crevasse height does not propagate to more than 60% of the glacier thickness (Jiménez and Duddu, 2018; Lai et al., 2020). Because it is assumed that crevasses propagate quickly from large tensile rates (Cuffey and Patterson, 2010, pp 450-451), we treat ice as an elastic solid (Luckman et. al., 2012). LEFM calculates a stress intensity factor (K_I). The theory is that as long as this stress intensity factor is greater than a fracture criterion, or ice toughness, then a crack will propagate assuming the presence of a small (.5—2.0 m) starter crack (Rist et al., 1996; van der Veen, 1998).

$$K_I = \int_0^h \frac{2\sigma_n(z)}{\sqrt{\pi h}}\, G(\gamma, \lambda)\, dz \tag{2}$$

$G(\gamma, \lambda)$ is a function of $\lambda = {}^{h}/_{H}$ and $\gamma = {}^{z}/_{h}$ established by fitting a polynomial curve to modelled stress intensity factor values (van der Veen, 1998). h is the crevasse height, H the ice thickness, and z the depth within the glacier where $z = 0$ at the glacier base and $z = H$ at the glacier surface:

$$G(\gamma, \lambda) = \frac{3.52(1-\gamma)}{(1-\lambda)^{3/2}} - \frac{4.35-5.28\gamma}{(1-\lambda)^{\frac{1}{2}}} + \left[\frac{1.30-0.03^{\frac{3}{2}}}{(1-\gamma)^{\frac{1}{2}}} + .83 - 1.76\gamma\right] \times [1-(1-\gamma)\lambda] \tag{3}$$

$\sigma_n(z)$ is the combined stresses (tensile, lithostatic, and water pressure) acting at the fracture's tip to either propagate or close the crevasse:

$$\sigma_n(z) = -\rho_i g(H-z) + \frac{\rho_i - \rho_s}{C} g\left[1 - e^{-C(H-z)}\right] + \rho_w g\left(H_p - z\right) + R_{xx}(z) \tag{4}$$

The first two terms in equation 4 make up the lithostatic stress; the second term is an empirical relation for ice density (van der Veen, 1998); ρ_s is the density of snow, 350 kg m^{-3}, g is the gravitational potential is 9.8 m/s^2 and C, a constant, is 0.02 m^{-1} after van der Veen (2013, p. 223). The third term is the basal water pressure where H_p is the piezometric head. The last term in equation 4 is the tensile stress. There are no direct measurements of tensile stress, so we modeled it from the strain rates during flooding event velocities and normal flow velocities. The strain rates are related to the tensile stress using van der Veen and Whillans (1989)'s glacier ice flow law through the rate factor. We treated the strain rates are treated as non-varying with depth because of the assumption that basal crevasses form at the grounding line where ice is floating. Increased speeds from the 2006 flooding event also increased the strain rates which is the largest influence on resulting basal crevasse heights (van der Veen, 1998) (see Figure S5).

We used Hooke (1981)'s rate factor as varying with depth which we calculated with Sandhäger et. al., (2005)'s depth-varying temperature profile with estimated surface and bottom temperatures of -20°C (van der Veen et al. 2014) and -1.9°C (Tinto et al., 2019) respectively. We estimate basal crevasse heights assuming a critical toughness value of .155 $MPa\ m^{1/2}$ because, to the best of our knowledge, it is the only measured ice toughness value from an Antarctic ice shelf (Rist et al., 1999). This toughness value was determined from an ice core sample from the Ronne Ice Shelf (Rist et al. 1999), but considering Byrd Glacier and the grounding line of the Ronne Ice Shelf have similar surface temperatures (Comiso et al, 2017), and ice thicknesses (Fretwell et al. 2013), we assume it is appropriate to use the same criterion.

LEFM calculations were applied to gridded point data over a ~20x30 km region within the grounding zone. The differing parameters at each point were strain rates and ice thickness values. The resulting basal crevasse heights were then interpolated in ArcMap using ordinary kriging to a new grid of 500 m spatial resolution (the same as the CReSIS grid).

Text S6. Subglacial water pathways

It is beyond the scope of this study to identify whether the type of subglacial water flow is channelized or film, and we do not include an analysis of a coupled hydrology and glacier dynamic model. We are interested to know the approximate locations of subglacial flood pathways to show that water from lakes will indeed drain at the Byrd Glacier grounding line and not at another outlet glacier. The grounding line exit location is also likely where freshwater plumes form and cause localized melt features in Antarctic ice shelves (Jenkins, 2011; Carter and Fricker, 2012; Le Brocq et. al., 2013; Marsh et. al., 2015).

Basal water pathways are estimated using a similar method to Livingstone et. al., (2013) which relies on the ArcGIS 10.6 toolset to derive hydrological pathways (based on O'Callaghan and Mark (1984)'s method). Water routes follow the direction of the largest hydraulic gradient which is estimated from Shreve (1972):

$$\Phi_h = \rho_i g h + (\rho_w - \rho_i) g (h - H) \quad (5)$$

The hydraulic gradient is then used to solve for the hydraulic head (Cuffey and Patterson, 2010 p.194):

$$Q = \frac{\Phi_h}{\rho_w g} \quad (6)$$

The hydraulic head is plugged in an 8-directional flow model by Jenson and Domingue (1988) to estimate the direction of subglacial water flow. The final step is estimating the flow accumulation which produces probable basal water pathways (Figure S6).

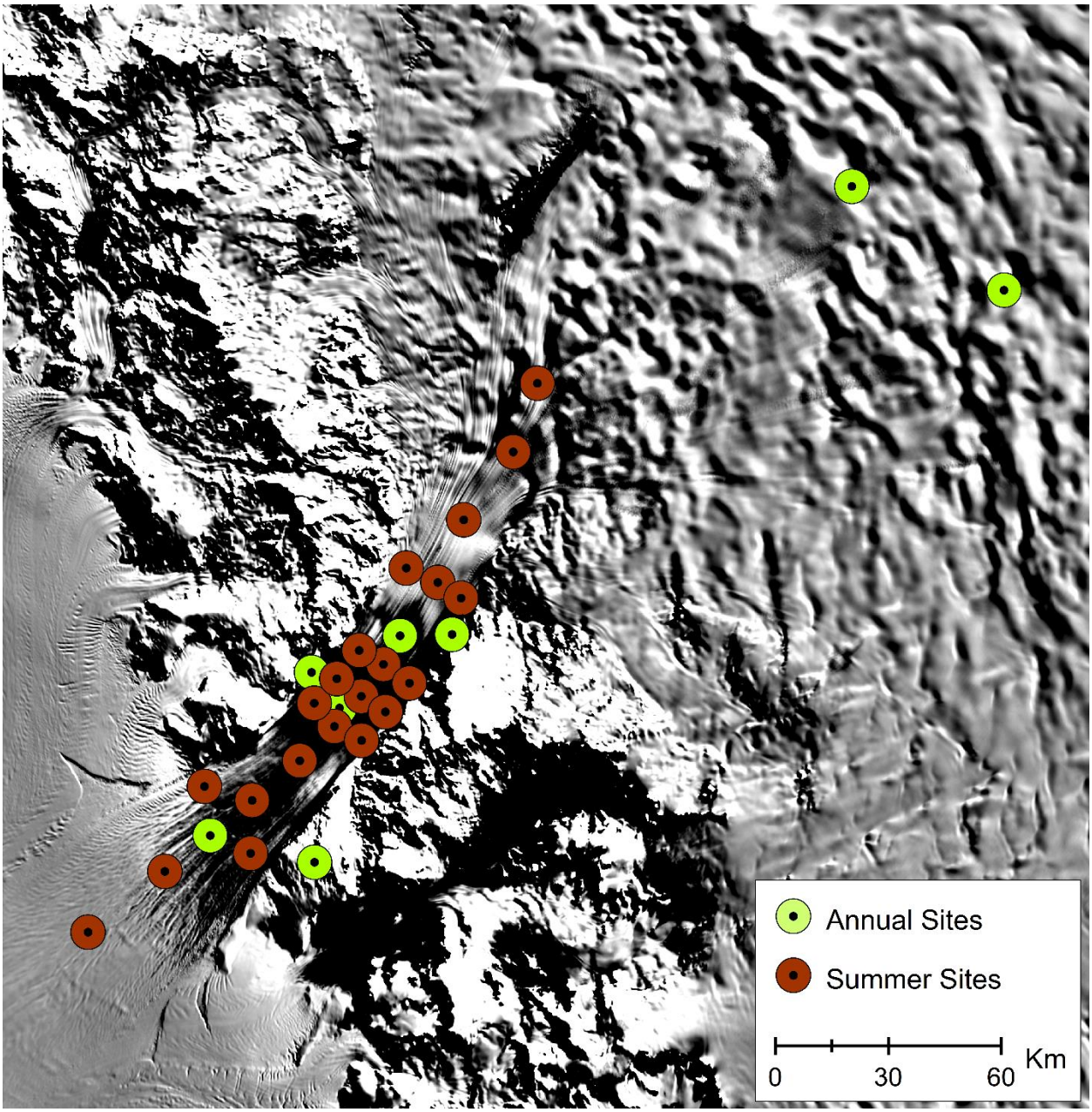

Figure S1. A map of the 29 GPS receivers deployed on Byrd Glacier from the two subglacial lakes to the floating portion on RIS over the duration of 2010-2013. The background image is from Haran et al. (2014) and available from NSIDC.

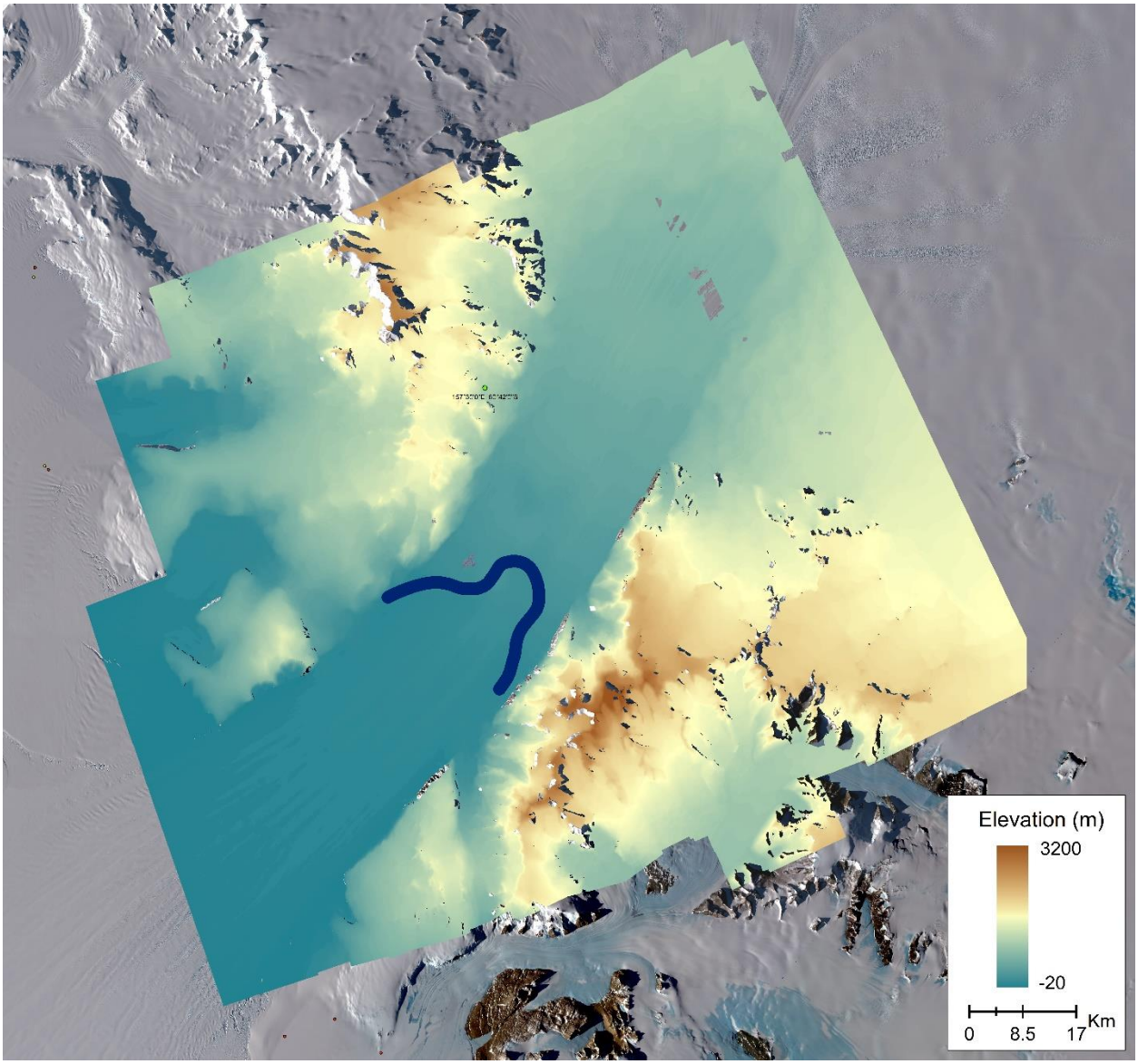

Figure S2. The final REMA DEM strip mosaic. The background is a band composite of Landsat 8 OCI's LC08_L1GT_047118_20190217_20190222_01_T2 and LC08_L1GT_047119_20190217_20190222_01_T2.

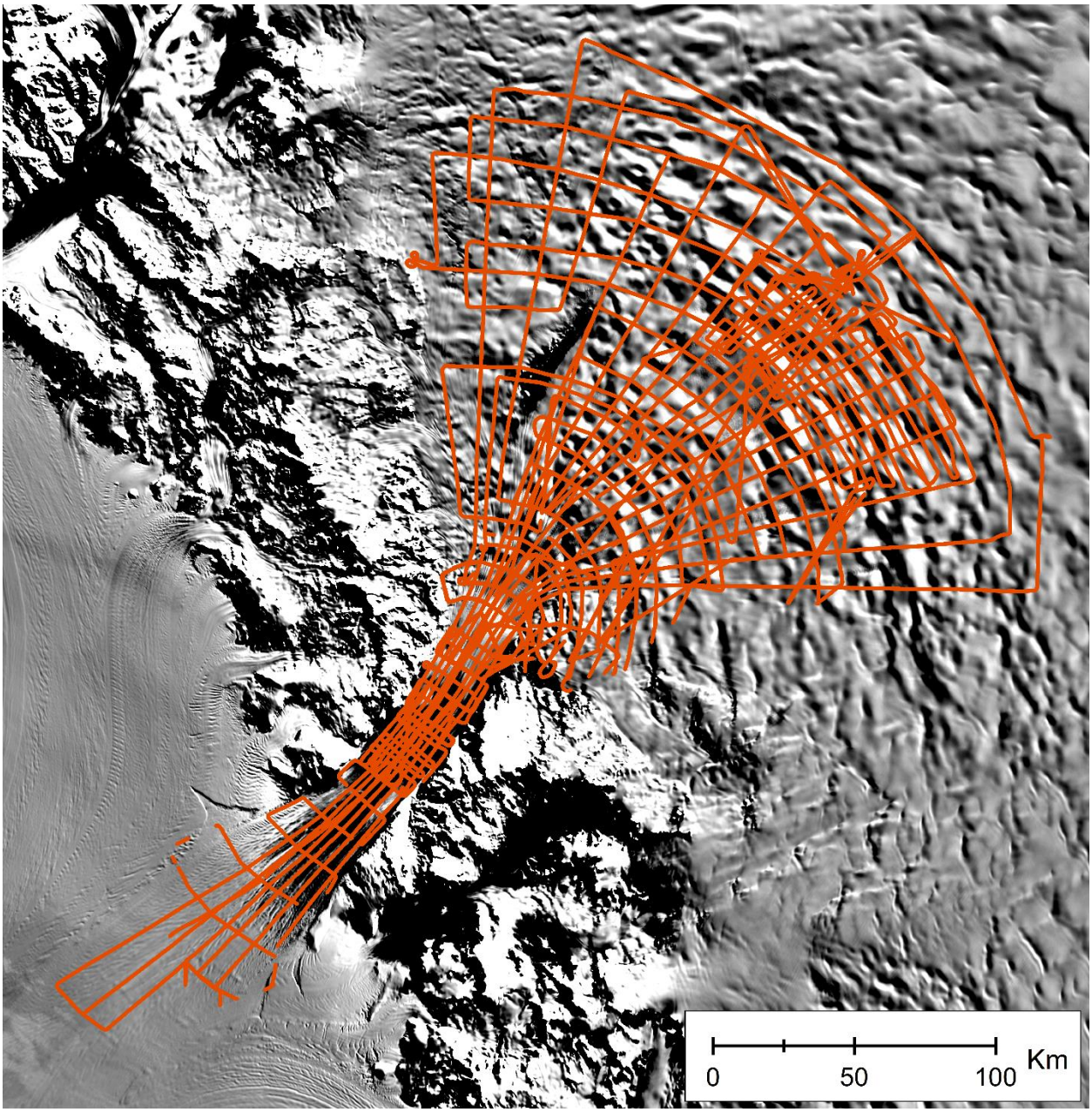

Figure S3. CReSIS flight paths in orange from the 2011-12 data collection over Byrd Glacier. All of the data used in this study are concentrated to the lower half of the glacier. These are the data used to generate the bedrock grid. The background image is from Haran et al. (2014) and available from NSIDC.

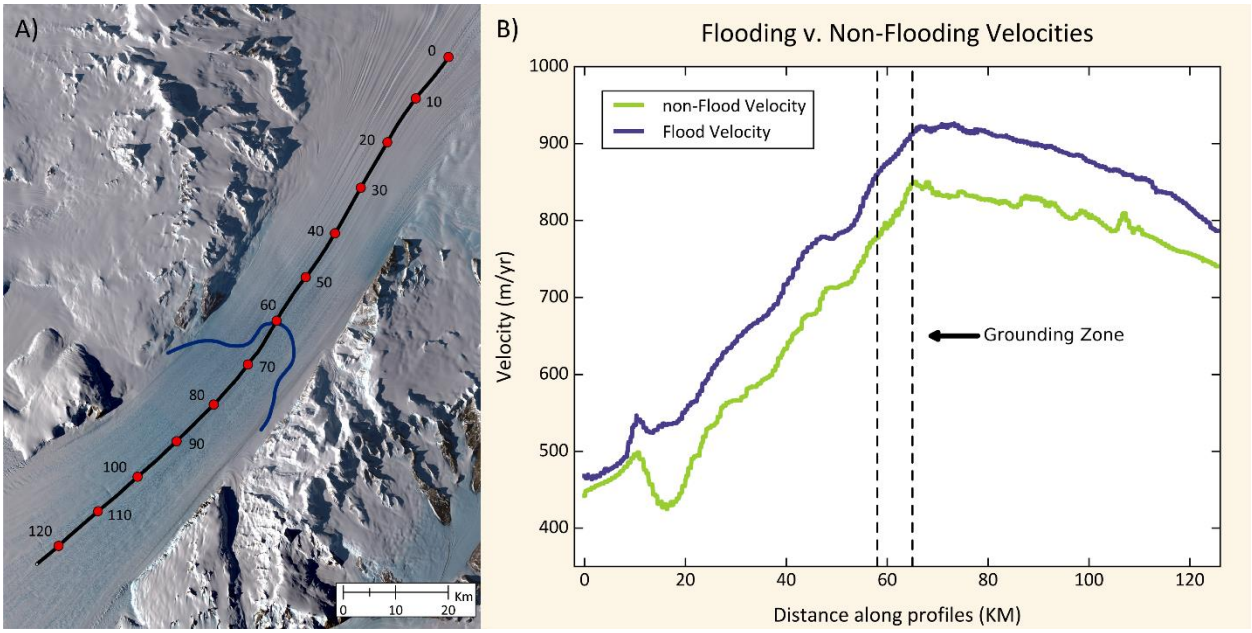

Figure S4. Plot of surface velocities (B) from a flooding period and a non-flooding period along a flow-path (A).

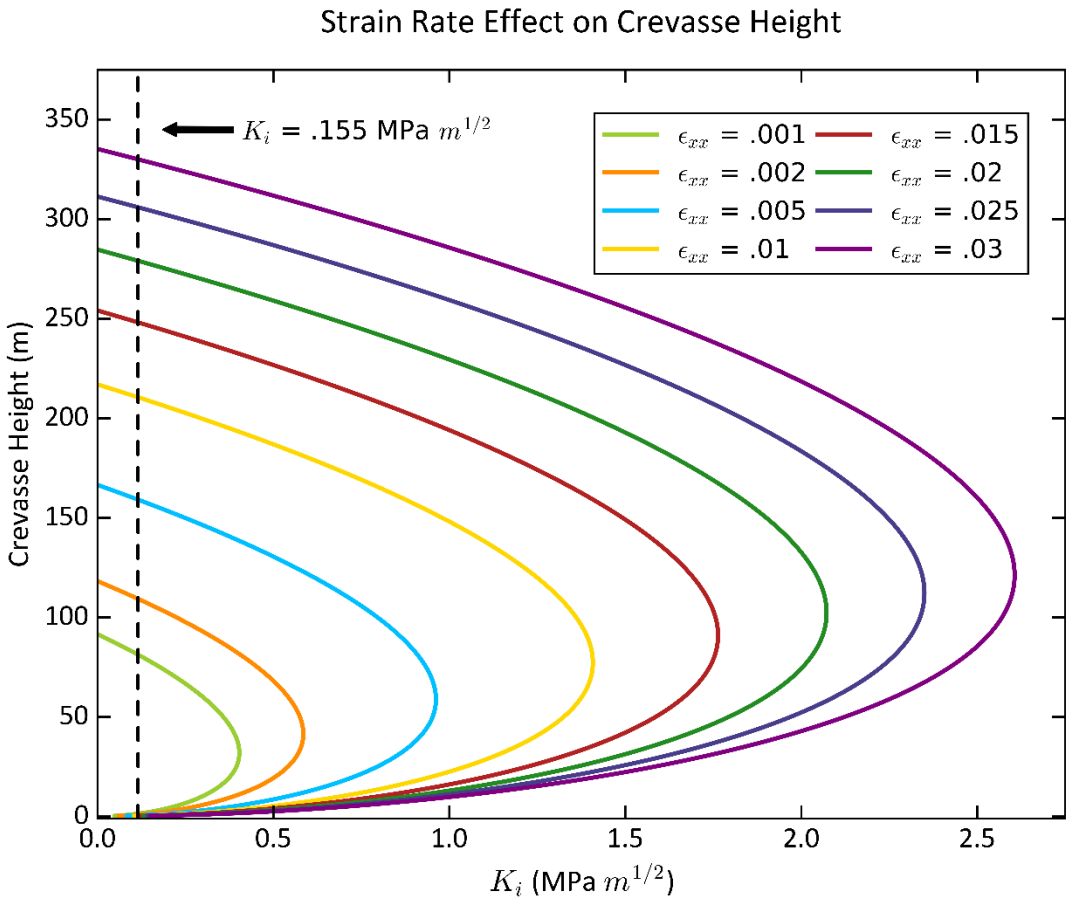

Figure S5. Crevasse height results with varying strain rates. Strain rate (ε_{xx}) values are in units of meters per year. In this example, the average ice thickness value within Byrd Glacier's grounding zone of 1,800 m was used. We estimated crevasse heights with the same stress intensity value of .155 $MPa\ m^{1/2}$(black dashed line), measured by Rist et al., (1999), from the Ronne Ice Shelf.

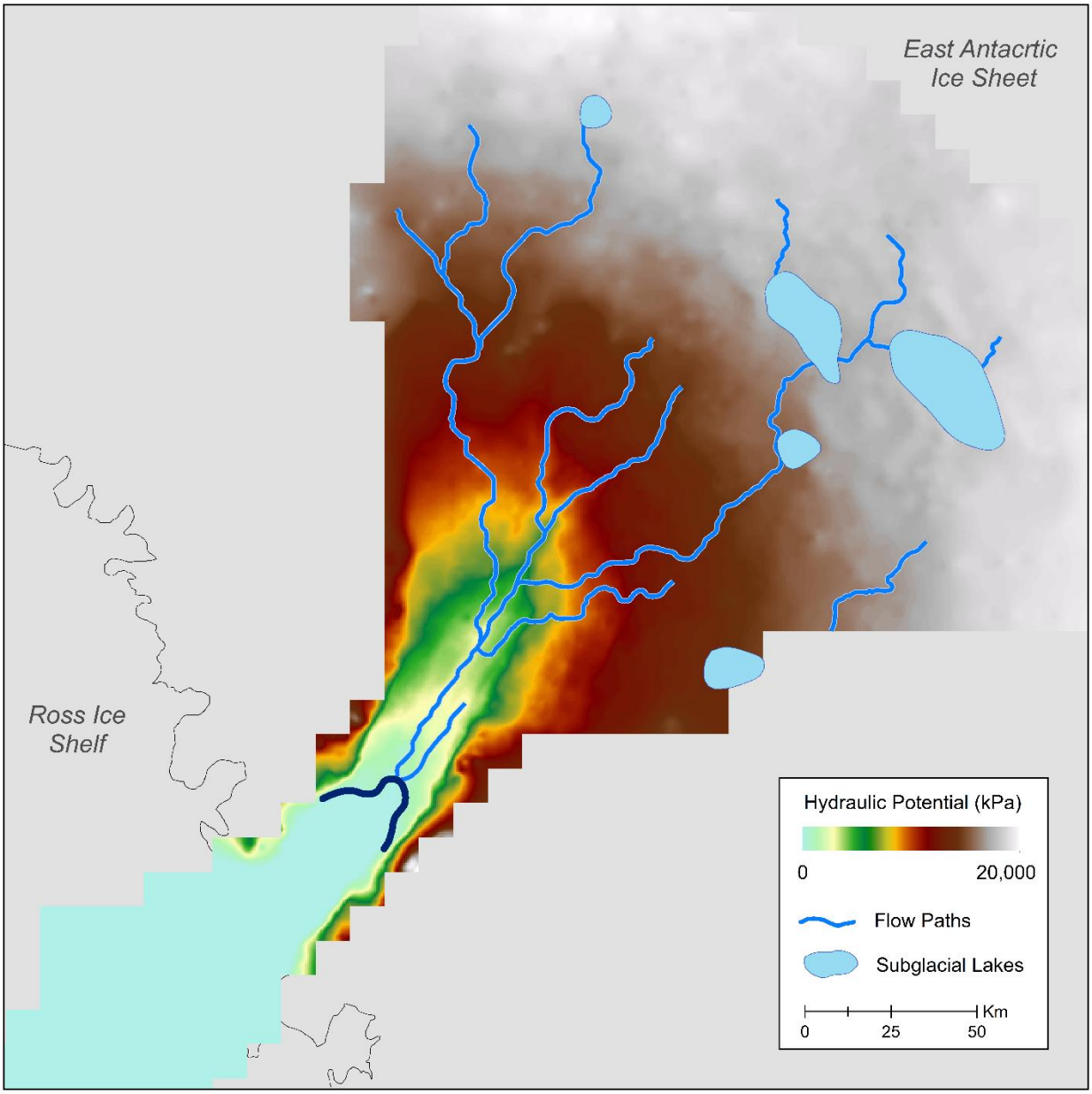

Figure S6. Map of hydraulic potential over Byrd Glacier's catchment basin to the grounding line. The subglacial lake locations are from Smith et al. (2009) and the light blue lines represent the path of substantial water flow.

REMA 2 m Strips
WV01_20170117_102001005B5DCE00_102001005D03ED00_seg1_2m_dem.tif
WV01_20161022_10200100572C2600_102001005728F300_seg1_2m_dem.tif
WV02_20170114_1030010063357E00_103001006328C800_seg1_2m_dem.tif
WV02_20170112_1030010063C79200_1030010064666E00_seg1_2m_dem.tif
WV02_20161104_103001005E85A100_1030010061CB4700_seg1_2m_dem.tif
WV03_20170106_1040010026CC6900_10400100263B2100_seg1_2m_dem.tif
WV02_20161106_103001005DB42D00_103001005D998800_seg1_2m_dem.tif
WV02_20161104_103001005FB39200_103001005F580E00_seg1_2m_dem.tif
WV02_20161103_103001005D2CB600_103001005F7E5300_seg3_2m_dem.tif
WV01_20170112_102001005E897C00_1020010059681600_seg1_2m_dem.tif
WV01_20170220_102001005BB1E700_102001005B62C700_seg1_2m_dem.tif
WV03_20170220_1040010029C88300_1040010029A3F500_seg1_2m_dem.tif
WV01_20170106_10200100596C6200_1020010059CA5F00_seg1_2m_dem.tif
WV01_20161105_10200100596C1200_102001005681D700_seg1_2m_dem.tif
WV01_20170112_102001005D748700_102001005DAFDE00_seg1_2m_dem.tif
WV02_20160204_1030010050525F00_1030010051D1C200_seg1_2m_dem.tif
WV01_20161107_102001005A3DD700_1020010056A10100_seg1_2m_dem.tif
WV01_20160204_1020010049146A00_1020010047BD2A00_seg1_2m_dem.tif
WV01_20170121_102001005AC91A00_102001005A582200_seg1_2m_dem.tif
WV03_20170123_104001002827D100_104001002891ED00_seg1_2m_dem.tif
WV01_20160201_102001004ACC8100_10200100468C3C00_seg1_2m_dem.tif
WV01_20160120_10200100487B0B00_102001004C1AF200_seg1_2m_dem.tif
WV01_20170122_102001005A724300_10200100594FD400_seg1_2m_dem.tif
WV01_20170130_102001005C044C00_102001005C1ACD00_seg1_2m_dem.tif
WV03_20161103_10400100239D2200_10400100231A1300_seg1_2m_dem.tif
CReSIS Data
Data_20111201_05_005
Data_20111205_08_003
Data_20111214_02_010
Data_20111214_02_012
Data_20111214_06_002
Data_20111214_06_003
Data_20111214_06_004
Data_20111216_03_002
Data_20111216_04_001
Data_20111216_04_003
Data_20111218_01_002
Data_20111218_01_003
Data_20111218_03_003
Data_20111218_03_005
Data_20111218_03_006

Data_20111218_03_007
Data_20111218_04_001
Data_20111218_04_009
Data_20111218_05_001
Data_20111218_05_003
CReSIS Point Data
Byrd_2011_Composite
Landsat 8 OLI Scenes
LC08_L1GT_046117_20161202_20170317_01_T2_B8.TIF
LC08_L1GT_047116_20161209_20170317_01_T2_B8.TIF
LC08_L1GT_047117_20170110_20170311_01_T2_B8.TIF
LC08_L1GT_048116_20170202_20170215_01_T2_B8.TIF
LC08_L1GT_048117_20170202_20170215_01_T2_B8.TIF
LC08_L1GT_048118_20170202_20170215_01_T2_B8.TIF
LC08_L1GT_049117_20170124_20170311_01_T2_B8.TIF
LC08_L1GT_050115_20170216_20170228_01_T2_B8.TIF
LC08_L1GT_050116_20170216_20170228_01_T2_B8.TIF
LC08_L1GT_050117_20161112_20170318_01_T2_B8.TIF
LC08_L1GT_050118_20161214_20170316_01_T2_B8.TIF
LC08_L1GT_051115_20170223_20170301_01_T2_B8.TIF
LC08_L1GT_051116_20170223_20170301_01_T2_B8.TIF
LC08_L1GT_051117_20170223_20170301_01_T2_B8.TIF
Velocity Data
lisa750_2016183_2017120_0000_0400_v1

Table S1. A list of all the data sets, not including the GPS data from the 2010-2013 field seasons, used in the analysis of this research. Information to access these data is in the acknowledgements section of the main text.

SI References (also listed in main text Reference section)

Carter, S. P., Fricker, H. A., and Siegfried, M. R. (2017). Antarctic subglacial lakes drain through sediment-floored canals: theory and model testing on real and idealized domains. *The Cryosphere*, *11*(1), 381-405.

Comiso, J.C., Gersten, R.A., Stock, L.V., Turner, J., Perez, G.J. and Cho, K. (2017). Positive trend in the Antarctic sea ice cover and associated changes in surface temperature. *Journal of Climate*, *30*(6), 2251-2267.

CReSIS. (2014). Antarctica 2011 Twin Otter Data, Lawrence, Kansas, USA. Digital Media. Retrieved from http://data.cresis.ku.edu/.

Cuffey, K. M., and Paterson, W. S. B. (2010). *The physics of glaciers*. Academic Press. pp. 194, 450-451.

Elosegui, P., J. L. Davis, J. M. Johansson, and I. I. Shapiro. (1996). Detection of Transient Motions with the Global Positioning System. *Journal of Geophysical Research: Solid Earth, 101*(B5), 11249–11261.

Elosegui, P., Davis, J. L., Oberlander, D., Baena, R., and Ekström, G. (2006). Accuracy of High-Rate GPS for Seismology. *Geophysical Research Letters, 33*(11).

Fahnestock, M., T. Scambos, T. Moon, A. Gardner, T. Haran, and M. Klinger. (2016). Rapid large-area mapping of ice flow using Landsat 8, *Remote Sensing of Environment, 185*. 84-94. https://doi.org/10.1016/j.rse.2015.11.023

Fretwell, P., Pritchard, H.D., Vaughan, D.G., Bamber, J.L., Barrand, N.E., Bell, R., Bianchi, C., Bingham, R.G., Blankenship, D.D., Casassa, G. and Catania, G. (2013). Bedmap2: improved ice bed, surface and thickness datasets for Antarctica. *The Cryosphere*, *7*(1), 375-393.

Glennie, C. (2018). Arctic high-resolution elevation models: Accuracy insloped and vegetated terrain. *Journal of Surveying Engineering 144*(1).

Gogineni, S., Yan, J.-B., Paden, J. D., Leuschen, C. J., Li, J., Rodriguez-Morales, F., Braaten, D.A., Purdon, K., Wang, Z., Liu, W. and Gauch, J. (2014). Bed topography of Jakobshavn Isbræ, Greenland, and Byrd Glacier, Antarctica. *Journal of Glaciology, 60*(223), 813-833.

Haran, T., Bohlander, J., Scambos, T. Painter, T., and Fahnestock, M. (2014). *MODIS Mosaic of Antarctica 2008-2009 (MOA2009) Image Map, Version 1 (updated 2019)*. Boulder, Colorado USA. NASA National Snow and Ice Data Center Distributed Active Archive Center. [October 9, 2019].

Hooke, R. LeB. (1981). Flow law for polycrystalline ice in glaciers: comparison of theoretical predictions, laboratory data, and field measurements. *Reviews of Geophysics*, *19*(4), 664-672.

Howat, I.M., Porter, C., Smith, B.E., Noh, M.J., and Morin, P. (2019). The reference elevation model of Antarctica. *The Cryosphere*, *13*(2), 665-674.

Jenkins, A. (2011). Convection-driven melting near the grounding lines of ice shelves and tidewater glaciers. *Journal of Physical Oceanography*, *41*(12), 2279-2294.

Jenson, S. K. and Domingue, J. O. (1988). Extracting topographic structure from digital elevation data for geographic information system analysis. *Photogrammetric engineering and remote sensing*, *54*(11), 1593-1600.

Jimenez, S. and Duddu, R. (2018). On the evaluation of the stress intensity factor in calving models using linear elastic fracture mechanics. *Journal of Glaciology*, *64*(247), 759-770.

Lai, Ching-Yao, Kingslake, J., Wearing, M. G., Chen, P-H. C., Gentine, P., Li, H., Spergel, J. J., and van Wessem, J. M. (2020). Vulnerability of Antarctica's Ice Shelves to Meltwater-Driven Fracture. *Nature, 584*(7822), 574–578.

Le Brocq, A. M., Ross, N., Griggs, J. A., Bingham, R. G., Corr, H. F., Ferraccioli, F., and Jenkins, A. (2013). Evidence from ice shelves for channelized meltwater flow beneath the Antarctic Ice Sheet. *Nature Geoscience*, *6*(11), 945-948.

Lichten, S. M., and Border, J. S. (1987). Strategies for High-Precision Global Positioning System Orbit Determination. *Journal of Geophysical Research: Solid Earth 92*(B12), 12751–12762.

Livingstone, S., Clark, C., Woodward, J. and Kingslake, J. (2013). Potential subglacial lake locations and meltwater drainage pathways beneath the Antarctic and Greenland ice sheets. *Cryosphere*, *7*(6), 1721-1740.

Luckman, A., Jansen, D., Kulessa, B., Edward King, P., and Benn, D. (2012). Basal crevasses in Larsen C Ice Shelf and implications for their global abundance. *The Cryosphere*, *6*(1), 113-123.

Marsh, O. J., Fricker, H. A., Siegfried, M. R., Christianson, K., Nicholls, K. W., Corr, H. F., and Catania, G. (2016). High basal melting forming a channel at the grounding line of Ross Ice Shelf, Antarctica. *Geophysical Research Letters*, *43*(1), 250-255.

McNabb, R. (2019). PyBob Software, *Download available*: https://github.com/iamdonovan/pybob

Noh, M.-J., and Howat, I. M. (2015). Automated stereo-photogrammetric DEM generation at high latitudes: Surface extraction with tin-based search-space minimization (SETSM) validation and demonstration over glaciated regions. *GIScience Remote Sensing*, *52*(2), 198-217.

Nuth, C., and Kääb, A. (2011). Co-registration and bias corrections of satellite elevation data sets for quantifying glacier thickness change. *The Cryosphere*, *5*(1), 271-290.

O'Callaghan, J.F. and Mark, D.M. (1984). The extraction of drainage networks from digital elevation data. *Computer Vision, Graphics, and Image Processing*, *28*(3), 323-344.

Pavlis, N. K., Holmes, S. A., Kenyon, S. C., and Factor, J. K. (2012). The development and evaluation of the Earth Gravitational Model 2008 (EGM2008). *Journal of geophysical research: Solid Earth*, *117*(B4).

Rist, M., Sammonds, P., Murrell, S., Meredith, P., Doake, C., Oerter, H., and Matsuki, K. (1999). Experimental and theoretical fracture mechanics applied to Antarctic ice fracture and surface crevassing. *Journal of Geophysical Research: Solid Earth*, *104*(B2), 2973–2987.

Sandhäger, H., Rack, W. and Jansen, D. (2005). Model investigations of Larsen B Ice Shelf dynamics prior to the breakup. *FRISP Rep*, *16*, 5-12.

Scambos, T.A., Dutkiewicz, M.J., Wilson, J.C. and Bindschadler, R.A. (1992). Application of image cross-correlation to the measurement of glacier velocity using satellite image data. *Remote sensing of environment*, *42*(3), 177-186.

Scambos, T. A., Fahnestock, M., Moon, T., Gardner, A., and Klinger, M. (2019). Ice Speed of Antarctica (LISA), Version 1. [2016-2017]. Retrieved from http://385doi.org/10.7265/nxpce997.

Shreve, R.L. (1972). Movement of water in glaciers. *Journal of Glaciology*, *11*(62), 205-214.

Smith, B.E., Fricker, H.A., Joughin, I.R. and Tulaczyk, S. (2009). An inventory of active subglacial lakes in Antarctica detected by ICESat (2003–2008). *Journal of Glaciology*, *55*(192), 573-595.

Stearns, L.A., Smith, B.E., and Hamilton, G.S. (2008). Increased flow speed on a large East Antarctic outlet glacier caused by subglacial floods. *Nature Geoscience*, *1*(12), 827-831.

Stearns, L.A. (2007). Outlet glacier dynamics in east Greenland and East Antarctica.

Tinto, K. J., Padman, L., Siddoway, C. S., Springer, S. R., Fricker, H. A., Das, I., Caratori Tontini, F., Porter, D. F., Frearson, N. P., Howard, S. L., Siegfried, M. R., Mosbeux, C., Becker, M. K., Bertinato, C., Boghosian, A., Brady, N., Burton, B. L., Chu, W., Cordero, S. I., Dhakal, T., Dong, L., Gustafson, C. D., Keeshin, S., Locke, C., Lockett, A., O'Brien, G., Spergel, J. J., Starke, S. E., Tankersley, M., Wearing, M.G., and Bell, R. E. (2019). Ross Ice Shelf response to climate driven by the tectonic imprint on seafloor bathymetry. *Nature Geoscience*, *12*(6), 441-449.

Van der Veen, C. J. (1998). Fracture mechanics approach to penetration of bottom crevasses on glaciers. *Cold Regions Science and Technology,27*(3), 213-223.

Van Der Veen, C. J., and Whillans, I. M. (1989). Force budget: I. Theory and numerical methods. *Journal of Glaciology*, *35*(119), 53-60.

Van der Veen, C. J. (2013). *Fundamentals of glacier dynamics*. CRC press. 223

Van der Veen, C. J., Stearns, L. A., Johnson, J. T., and Csatho, B. M. (2014). Flow dynamics of Byrd Glacier, East Antarctica. *Journal of Glaciology,60*(224), 1053-1064.